Supporting Information:

TMDC Ternary Alloy based Triboelectric Nanogenerator with Giant Photo-induced Enhancement

Didhiti Bhattacharya[1], Shubhrasish Mukherjee[1], Rajib Kumar Mitra[1], Samit Kumar Ray[*1,2]

[1]S. N. Bose National Centre for Basic Science, Sector III, Block JD, Salt Lake, Kolkata – 700106

[2] Indian Institute of Technology Kharagpur, 721302, India

Email: physkr@phy.iitkgp.ac.in

Contents:

1. TEM images:

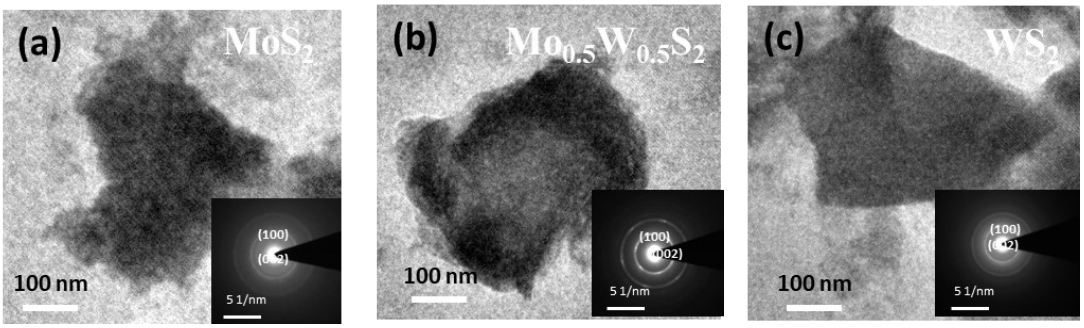

Figure S1: TEM images of (a) MoS_2, (b) $Mo_{0.5}W_{0.5}S_2$, (c) WS_2 nanosheets and selected area electron diffraction patterns (SAED) are shown inset.

2. E-DAX mapping of $Mo_{0.5}W_{0.5}S_2$ ternary alloy nanosheets:

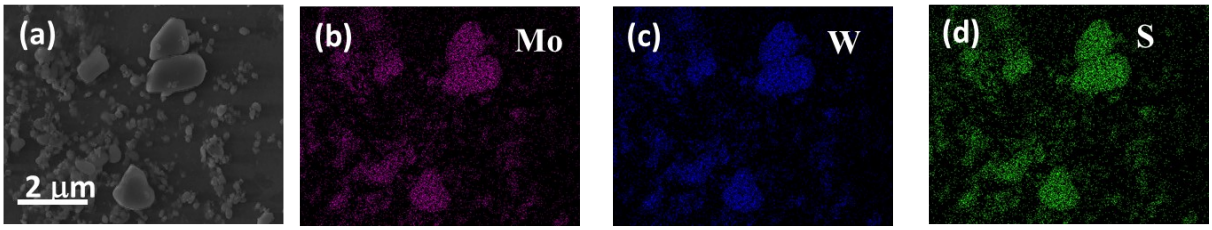

Figure S2: (a) FESEM image of $Mo_{0.5}W_{0.5}S_2$ nanosheets. E-DAX mapping of $Mo_{0.5}W_{0.5}S_2$ ternary alloy nanosheet indicating presence of (b) Mo, (c) W and (d) S elemental uniform distributions.

3. XRD and Raman study:

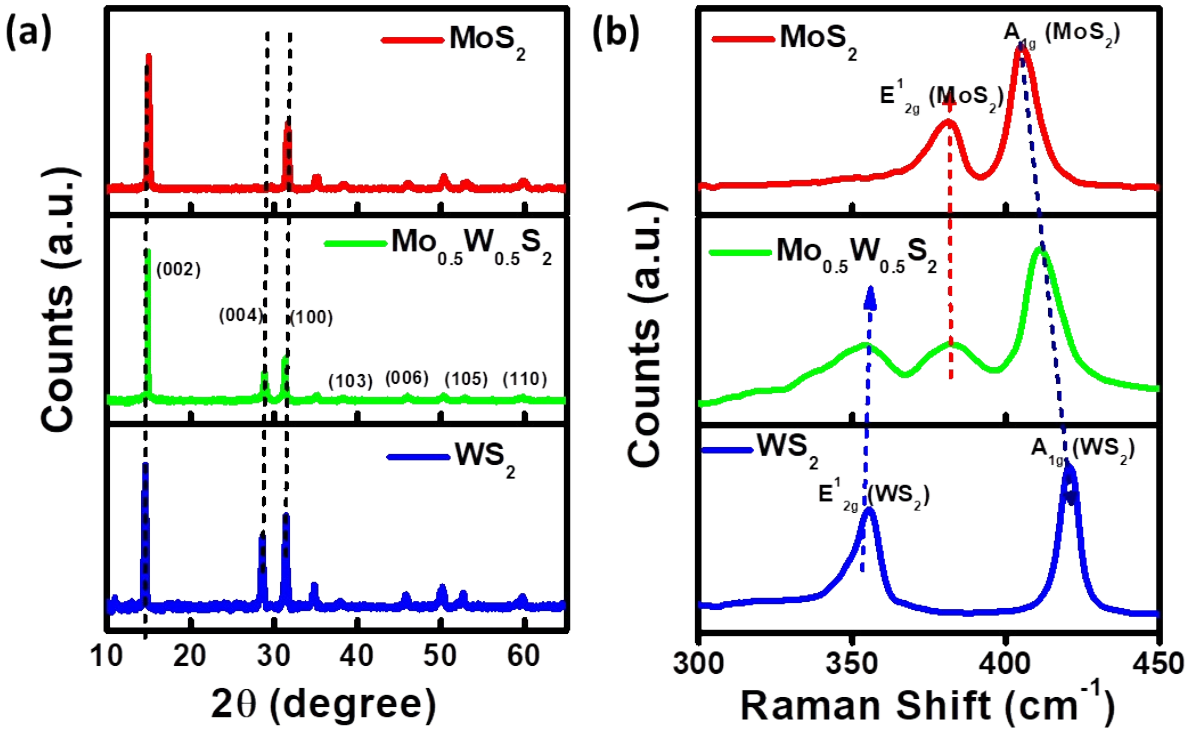

Figure S3: (a) XRD patterns and (b) Micro-Raman spectrums (Ex: 532 nm) of MoS_2, $Mo_{0.5}W_{0.5}S_2$, WS_2 nanosheets.

X-ray diffraction (XRD) pattern revels good crystallinity of all synthesized nanosheets and indicate the formation of lattice planes and are correlated with HRTEM analysis. In $Mo_{0.5}W_{0.5}S_2$ alloy three prominent Raman peaks are observed, E^1_{2g} modes for MoS_2 and WS_2, the overlapped peak A_{1g} for MoS_2 and WS_2. In this alloy the shift and broadening of E^1_{2g} and A_{1g} modes related Raman peaks than the binary counterparts are noticed. These are due to variation of effective mass, electron affinity, size of Mo and W and bond length variation of Mo-S, W-S and there relative strength modulation in alloy system.

4. **Absorbance and Photoluminescence Study:**

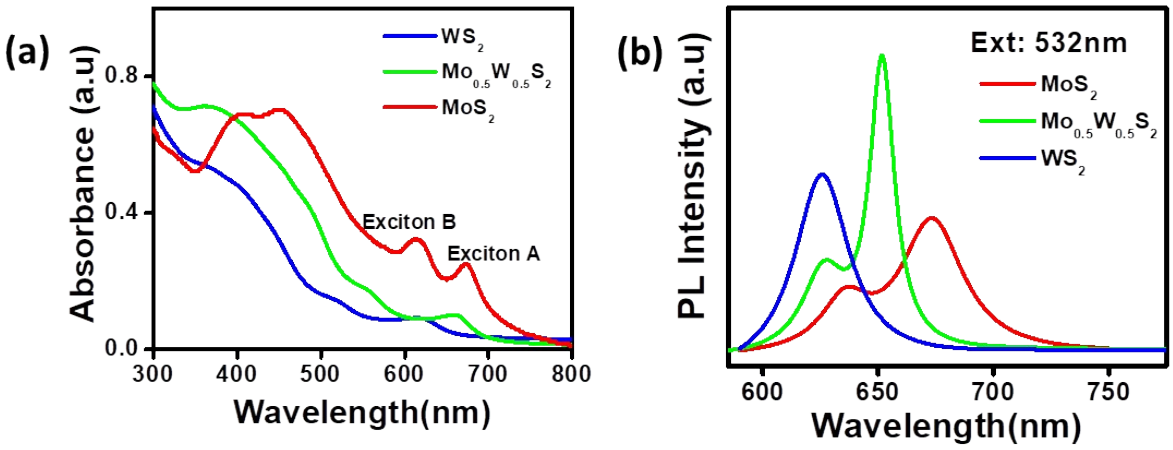

Figure S4: (a) Absorption and (b) Micro-Photoluminescence (Ex: 532 nm) spectrum of MoS_2, $Mo_{0.5}W_{0.5}S_2$, WS_2 nanosheet.

In the absorption spectra of all the samples exciton A and B peak is observed and exhibit red shift as the samples are varied from WS_2 to MoS_2, the separation between the excitonic peaks is enhanced from MoS_2 to WS_2, indicates the enhanced spin-orbit coupling strength. The red shift of photoluminescence peak position indicates the variation of optical band gap of the samples as those are varied from WS_2 to MoS_2.

5. **Conductive AFM Study:**

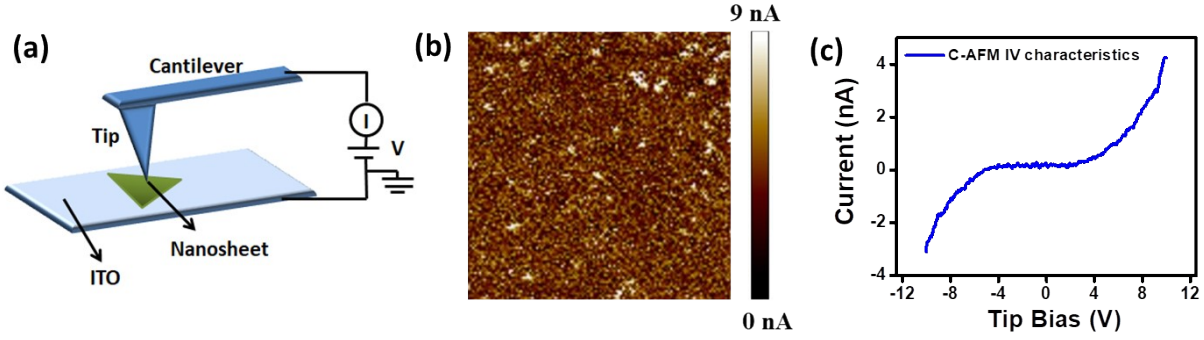

Figure S5: (a) Schematic of working mechanism of C-AFM, (b) C-AFM current mapping of $Mo_{0.5}W_{0.5}S_2$ nanosheet under bias 0 V. (c) Point contact I-V characteristic of $Mo_{0.5}W_{0.5}S_2$ alloy nanosheets.

TMDC $Mo_{0.5}W_{0.5}S_2$ alloy thin film is prepared by spin coating alloy nanosheets over ITO side of ITO-PET substrate and contact mode AFM is performed (Figure S5a). Pt/Ir coated conductive C-AFM tip is sliding over nanosheet surface and the friction induced tribocurrent

is generated and the topography of the surface current mapping is depicted in Figure S5b, this generated surface charge is needed for production of tribocharges during contact electrification. The charge transport between the tip and sample is induced by electronic excitation under friction and current-voltage (I-V) characteristic (Figure S5c) indicates the tip-sample interface plays a crucial role in energy harvesting. The I-V characteristic of these ternary alloy nanosheets with Pt/ Ir-coated conductive AFM tip is recorded in C-AFM mode, indicates the conductivity between the AFM tip and nanosheets also. With increasing applied bias, the current increases in both directions, indicating metal-semiconductor junction like charge transport between tip and sample surface.

6 Electrostatic Force Microscopy:

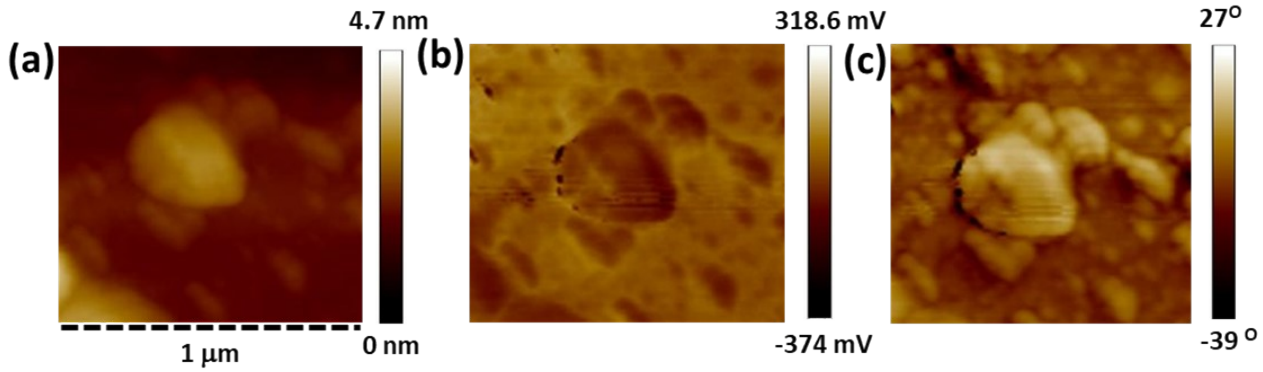

Figure S6: (a) Surface topography. Electrostatic Force Microscopy (EFM) images (b) Surface potential amplitude and (c) Phase contrast of $Mo_{0.5}W_{0.5}S_2$ nanosheet during scanning (with tip bias +3V).

For electrostatic force microscopy (EFM) TMDC $Mo_{0.5}W_{0.5}S_2$ alloy thin film (Figure S6a) is prepared by spin coating alloy nanosheets onto the top of Si/SiO_2 substrate. The EFM potential mapping (Figure S6b) reflects the generation of surface charge density due to tip to sample electrostatic interaction. EFM phase image (Figure S6c) is recorded simultaneously along with amplitude image and reveals noticeable phase contrast difference between alloy nanosheet and Si/SiO_2 substrate. Both the amplitude and phase mapping are originated due to electrostatic interaction between tip charges and charges accumulated at sample surface, whereas the electrostatic force is the combination of both coulombic and capacitive interactions.

7. Triboelectric Open-circuit Voltage Study:

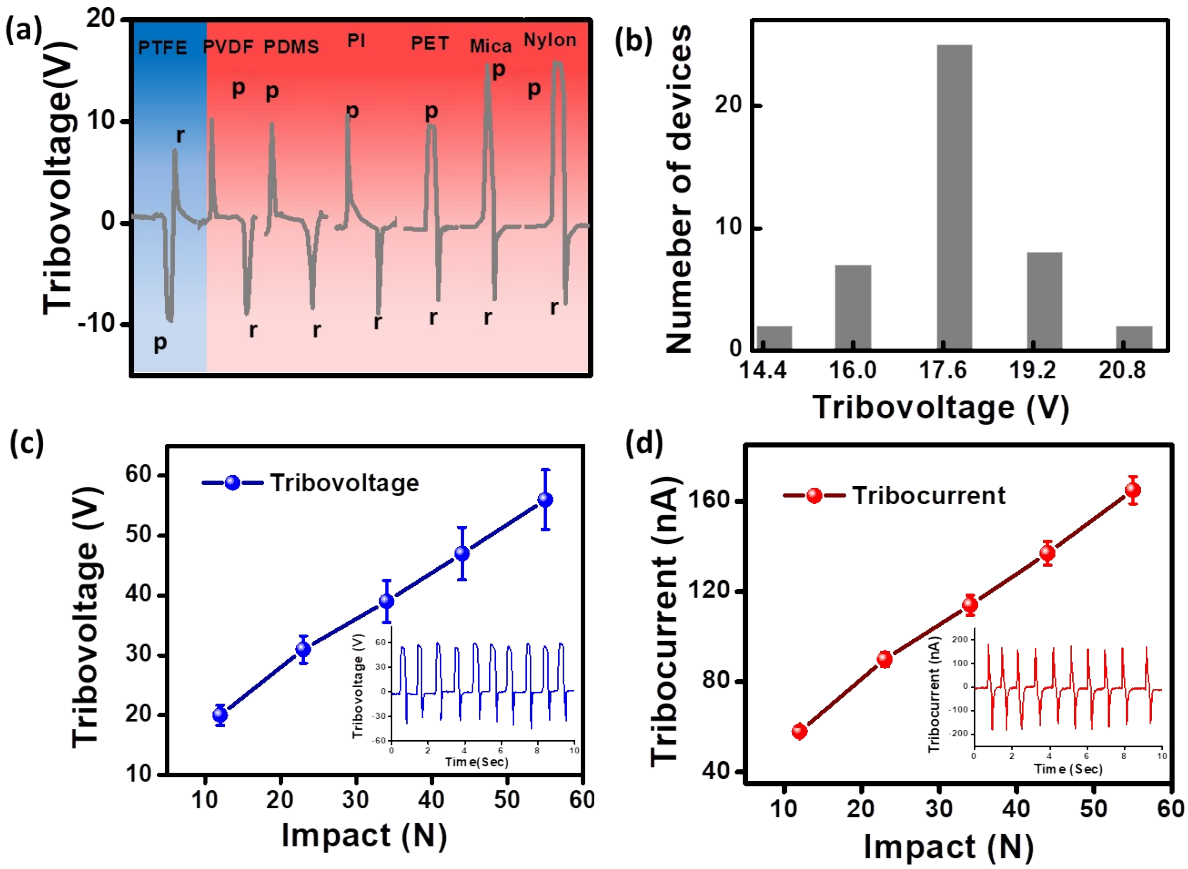

Figure S7: (a) Triboelectric charging behaviour of $Mo_{0.5}W_{0.5}S_2$ with different dielectric materials and the corresponding open-circuit output voltages, where p and r defines pressing and releasing actions. (b) Statistical distribution of open circuit output voltage from different TENG devices. Variation of (c) Open circuit tribo-voltage and (d) short circuit tribo-current with impact and tribooutputs from the $Mo_{0.5}W_{0.5}S_2$ –nylon TENG device under ~ 56 N impacts are shown inset respectively.

To investigate the charging positions of TMDC ternary alloy $Mo_{0.5}W_{0.5}S_2$ in the triboelectric series, several representative dielectrics with various charging affinities including PTFE, PVDF, PDMS, PET, PI, mica and nylon are selected to pair with TMDC layers in a vertical contact-separation TENG configuration. It is well recognized that the triboelectricity generation mechanism relies on the coupling of contact electrification and electrostatic induction effects.

During the pressing process, a positive voltage is observed and a negative voltage is observed during the releasing process for all configurations except $Mo_{0.5}W_{0.5}S_2$-PTFE. This indicates that the TMDC layer is positively electrified upon contacting with PTFE and for all

other dielectric pair $Mo_{0.5}W_{0.5}S_2$ is negatively electrified upon contact (marked as two different colours in Figure S7a). Thus, it is clear that these TMDC layers lie between PTFE and PVDF in the triboelectric series. To represent the polarity reversing we have highlighted two extrema cases for $Mo_{0.5}W_{0.5}S_2$-PTFE and $Mo_{0.5}W_{0.5}S_2$-nylon pairs in the main manuscript.

Figure S7c and d represent the open circuit tribo voltage and short circuit current at relatively higher impact. Here it is seen that the tribo-response increases monotonically with impact. Open-circuit tribovoltage is observed to be ~55V ($\mp$ 5V) (inset Figure S7c) and short-circuit tribocurrent is estimated to be ~ 165 nA ($\mp$ 6 nA) (inset Figure S7d) under an external mechanical impact of ~56 N. Though this TENG possess high mechanical endurance, there is a risk of material abrasion. So, to avoid any fluctuations of tribo-output under this high impact, we have done all the photo-coupled tribo measurements under a moderate impact regime (up to~7.6 N).

8. COMSOL Simulation:

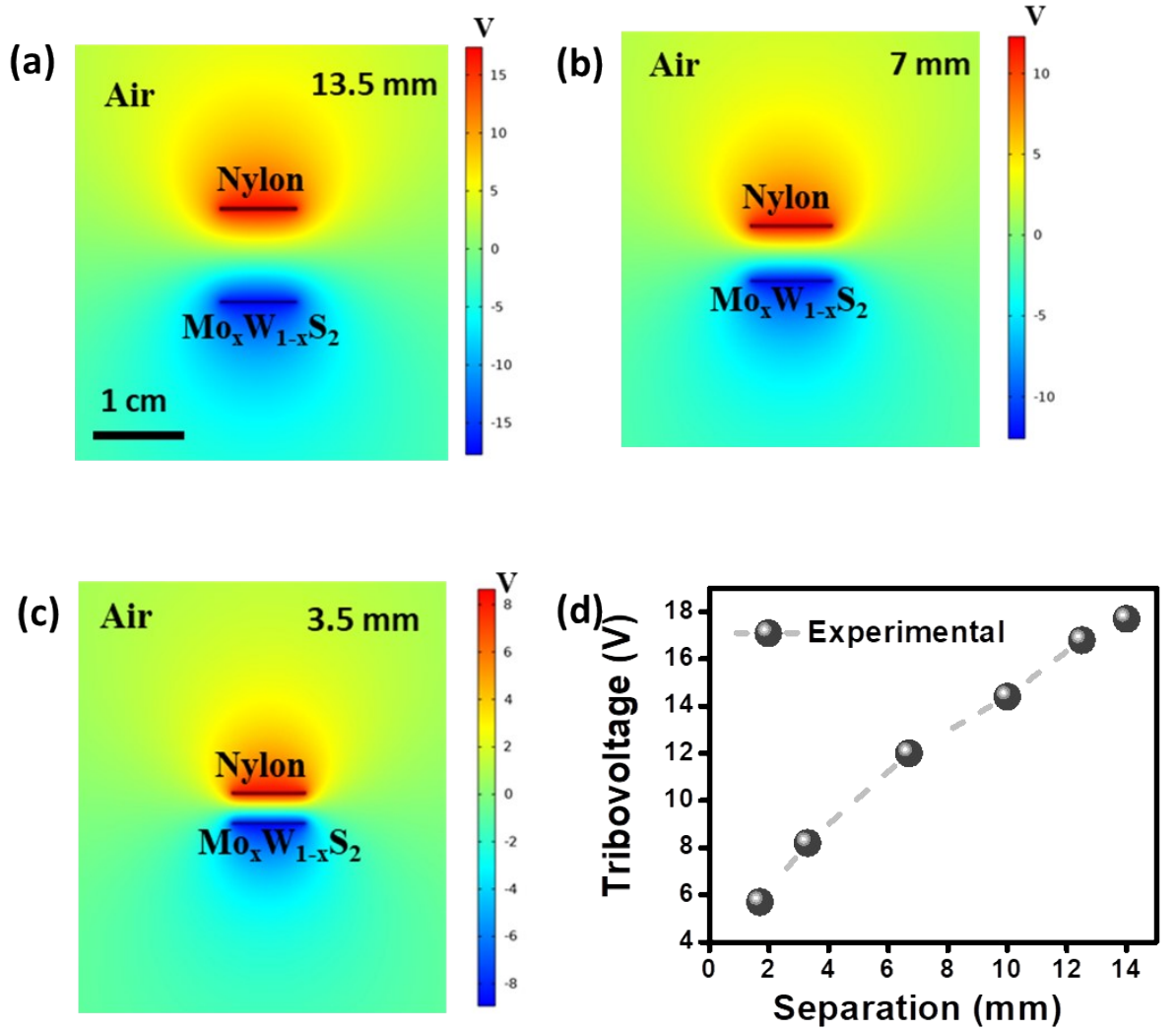

Figure S8: COMSOL simulation of Open circuit tribovoltage (V_{oc}) for varying spacer distance (a) 13.5 mm, (b) 7 mm, (c) 3.5 mm, (d) Variation of V_{oc} with varying separation between two dielectrics (experimentally).

By periodic the contact and separation of the two dielectrics, an alternative voltage is generated from this TENG. Corresponding simulations of potential distribution in three different separation distances by COMSOL are presented in Figure S8 a-c. The variation of output tribovoltage (experimental) with varying the separation between the two friction layers is depicted in Figure S8d.

The generated open circuit output voltage between the two electrodes in contact-separation mode is expressed as $Voc = \frac{\sigma d}{\in_o}$, where σ denotes the surface charge density and d is spacer layer thickness and $\in_o$ is free space permittivity. So the voltage is increased

linearly with gap distance upto a limiting saturation value for a specific configuration at a particular impact frequency.

9. Photocurrent Study of TMDC photodetector devices:

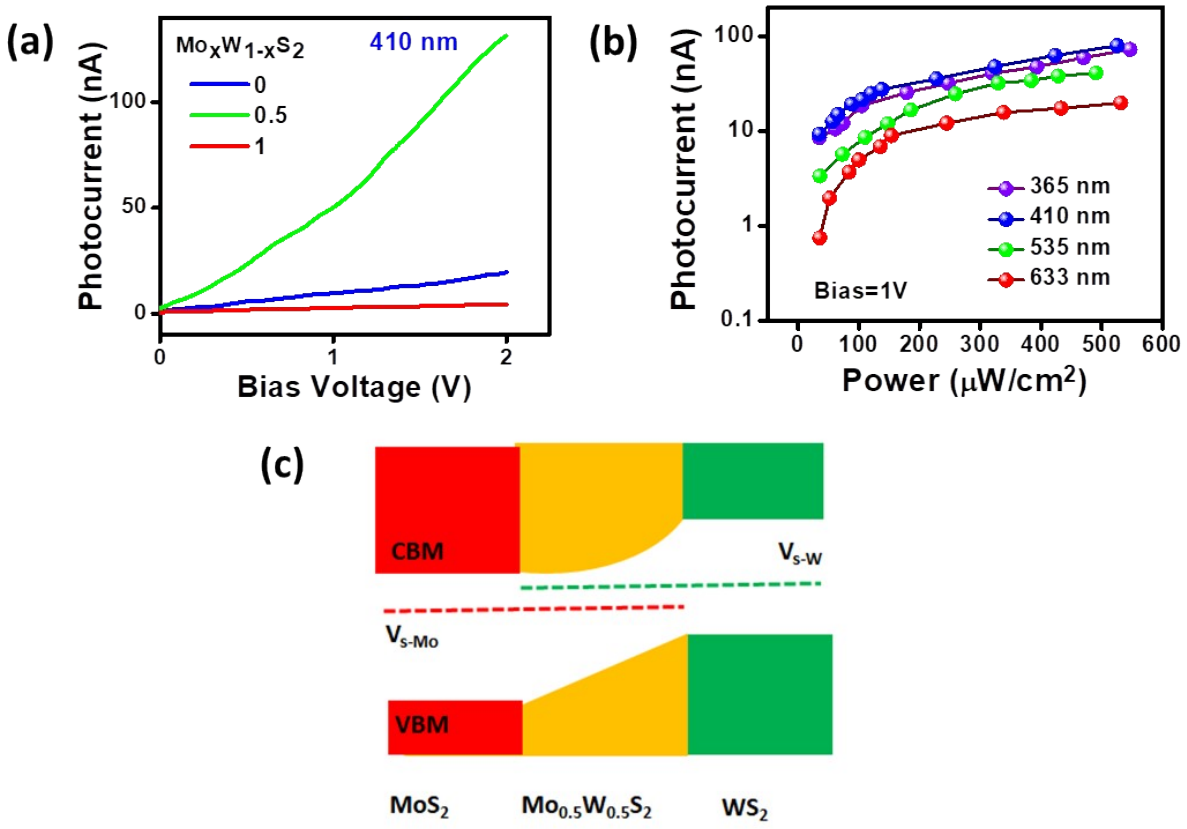

Figure S9: (a) Photocurrent-Bias Voltage characteristic of $Mo_xW_{1-x}S_2$ nanosheets (x=0, 0.5, 1) under 410 nm illumination. (b) Variation of Photocurrent of $Mo_{0.5}W_{0.5}S_2$ nanosheet with power under different illuminations (365 nm, 410 nm, 535nm and 633 nm) wavelengths. (c) Schematic band diagrams with localized defect states for MoS_2, ternary $Mo_{0.5}W_{0.5}S_2$, and WS_2 to explain the photocurrent enhancement in ternary alloy.

In MoS_2 (WS_2), there are S-vacancies are present around Mo (W) atoms and denoted as V_{Mo-S} and (V_{W-S}) and positioned inside the bandgap and act as scattering center of carriers and hampers transport and act as defect mediated recombination center for photogenerated carriers, reduces photocurrent. After alloying the energy band position gradually changes and for $Mo_{0.5}$ $W_{0.5}S_2$ alloy CBM lies between MoS_2 and WS_2, such that it is relatively near of MoS_2 but stays away from WS_2. But the energy level of defect states in the alloy in this $Mo_{0.5}W_{0.5}S_2$ alloy is similar position as binary counterparts. Due to CBM energy level realignment and vacancy induced defect states position, V_{W-S} defect states acts as shallow

level rather deep level defect states. In $Mo_{0.5}W_{0.5}S_2$ alloy the electrons are captured by $V_{W\text{-}S}$, instead of recombination with holes those electrons become free carriers again and go back to conduction band again. So for this deep to shallow level defect states conversion mechanism, suppression of defect states in $Mo_{0.5}W_{0.5}S_2$ alloy results higher photocurrent than binary counterparts.

10. <u>Comparative photosensitive tribo performance study:</u>

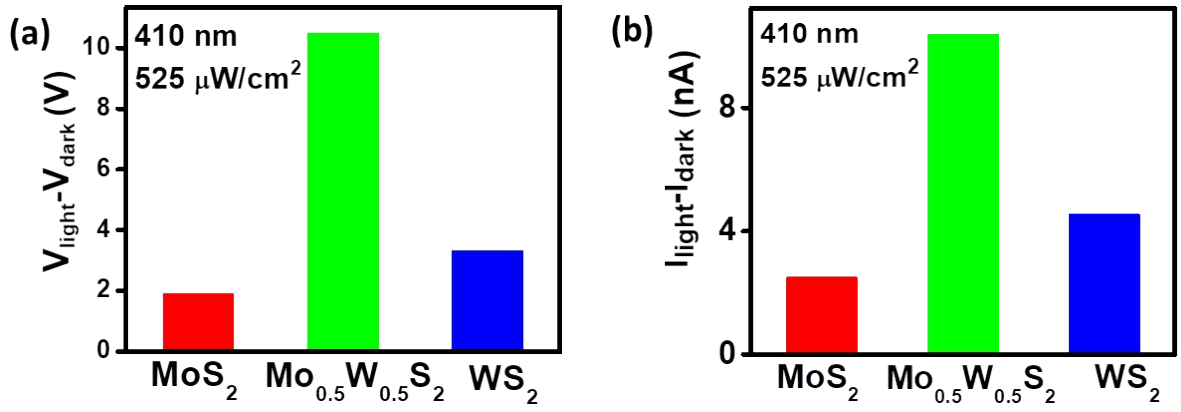

Figure S10: Comparison of photo enhanced (a) open-circuit output voltage and (b) short circuit current from the different $Mo_xW_{1-x}S_2$ (x=0, 0.5, 1)-nylon combination TENG device.

11. Tribocurrent under different illuminations:

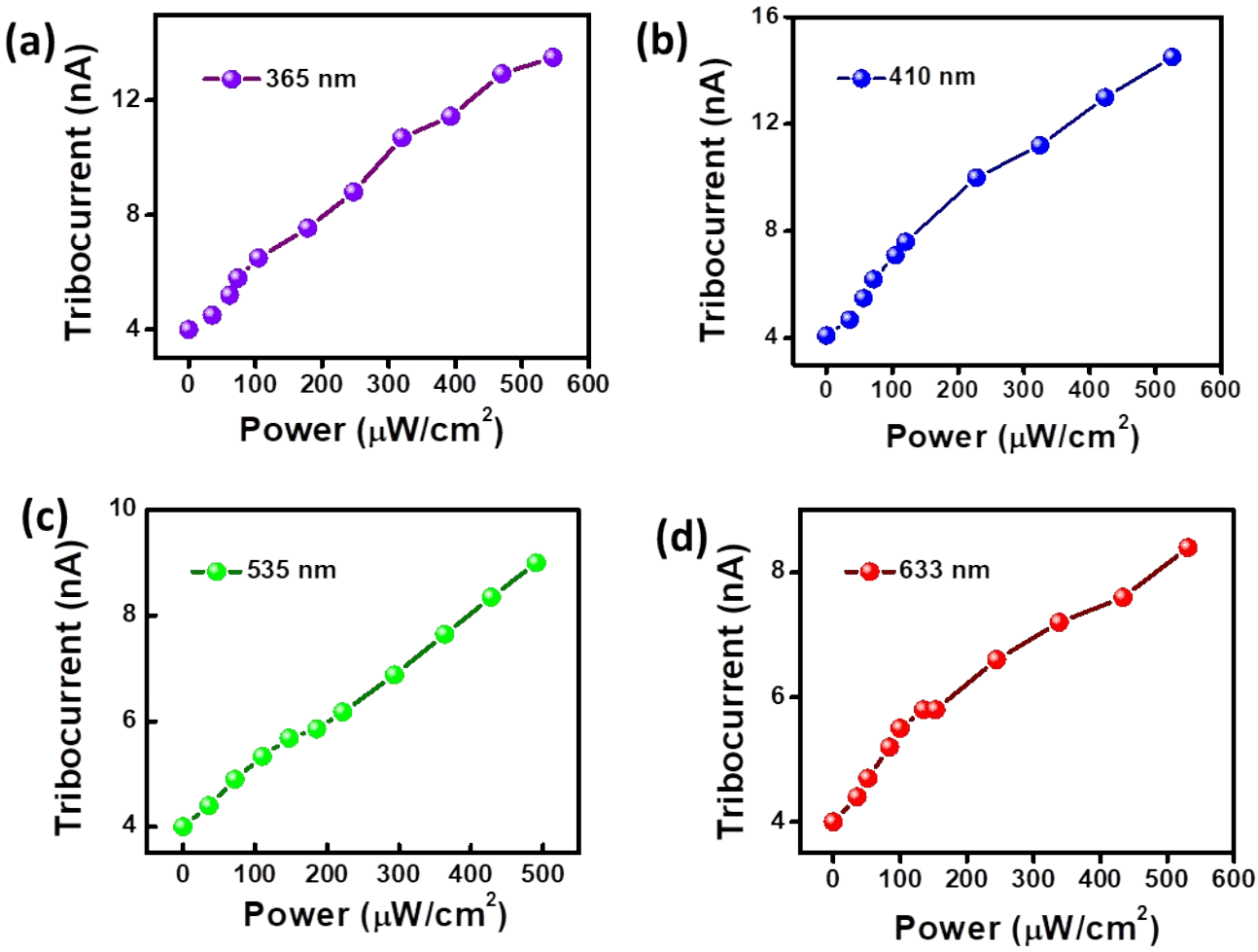

Figure S11: Variation of short circuit tribocurrent with varying illumination intensity under (a) 365 nm (b) 410 nm, (c) 535 nm and (d) 633 nm.

12. Stability and Flexibility Test

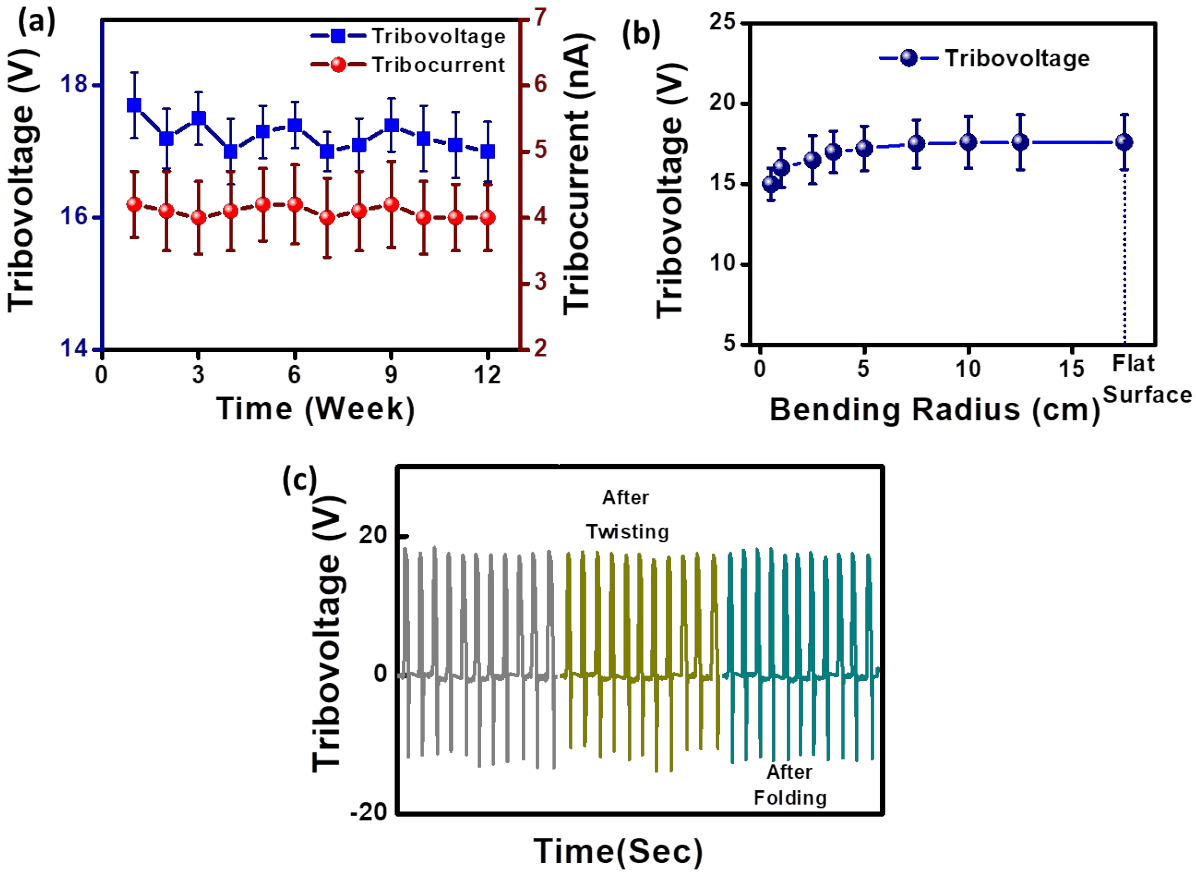

Figure S12: Variation of (a) open circuit tribovoltage (left axis) and short circuit tribocurrent (right axis), (b) tribo-voltage from the flexible TENG device when it is attached on different curved surface, (c) flexibility test of the TENG after different actions under 7.6 N impact applied force.

To test the flexibility of the TENG, this device is attached on the surfaces with different radius of curvature. The tribo outputs under a constant impact force (7.6 N) are measured. It is observed that the tribo-outputs remain nearly unaltered for the flat surface. Also, following twisting, folding of this TENG device, the output remains unchanged; indicating the superior flexibility and durability of the TENG device.